Diffusion of spherical particles in microcavities

A. Imperio,[1,a)] J. T. Padding,[2,b)] and W. J. Briels[1,c)]
[1]*Computational Biophysics, University of Twente, P.O. Box 217, Enschede 7500 AE, The Netherlands*
[2]*IMCN, Université catholique de Louvain, Croix du Sud 1, Louvain-la-Neuve, Belgium*

(Received 21 October 2010; accepted 24 March 2011; published online 18 April 2011)

The diffusive motion of a colloidal particle trapped inside a small cavity filled with fluid is reduced by hydrodynamic interactions with the confining walls. In this work, we study these wall effects on a spherical particle entrapped in a closed cylinder. We calculate the diffusion coefficient along the radial, azimuthal, and axial direction for different particle positions. At all locations the diffusion is smaller than in a bulk fluid and it becomes anisotropic near the container's walls. We present a simple model which reasonably well describes the simulation results for the given dimensions of the cylinder, which are taken from the recent experimental work. © *2011 American Institute of Physics*. [doi:10.1063/1.3578186]

I. INTRODUCTION

Modeling the motion of colloidal particles under confinement is of interest for many industrial applications which involve the entrapment of particles in microporous materials and diffusion controlled reaction mechanisms. An important class is that of coating processes where the particles have to diffuse toward a wall before being immobilized. Other applications involve microfluidic chips[1,2] and surface-based biosensor.[3] Furthermore, the confinement of particles in more than one dimension is relevant for the synthesis of colloids inside droplets[4] and for understanding the transport of proteins, lipid granules, and other macromolecular assemblies through a biological cell.

Most of the past work on modeling the mobility of a particle in confinement has focussed on a particle in proximity of a flat wall or within an infinitely long cylinder.[5–9] The motion of an arbitrarily shaped particle near boundaries has been studied in Ref. 10 while the settling of a particle inside a cylinder closed at the bottom but characterized by a free surface at the top has been analyzed in Ref. 11. Finally, for a historical perspective on the motion of a sphere in an incompressible fluid, from Stokes' law to Faxén's solution of the Navier–Stokes equations for particular bounded systems, see also Ref. 12. Under the assumption of creeping motion, previous investigations are mainly based on various approximate perturbative schemes, which are generally not valid when the size of the particle, the size of the cavity, and the gap between particle and wall are all comparable, which is the case we are interested in. Recently, however, a semianalytical procedure for the calculation of the mobility matrix of a spherical particle inside a cylinder has been presented in Ref. 13, which can be used under a wide range of confinement conditions.

The motion of a particle in a closed three-dimensional container has been studied less intensely. The flow field around a sphere has been studied in Refs. 14 and 15 in various confined geometries. The motion of a particle along the axis of closed cylinders and closed cones is discussed in Ref. 16, where experimental and theoretical results are presented for a millimeter sized sphere settling in a very viscous silicone oil. Agreement is found until the wall–particle separation is of the order of the particle diameter. Recently, the diffusion coefficients of micrometer-sized spheres moving in a squat cylinder containing a water solution has been studied,[17] showing that the diffusion is strongly affected by the confinement and substantial corrections to the Stokes' law are required.

The analysis of the motion of a particle inside a cavity can be based upon the solution of Navier–Stokes equations under particular regimes, such as the creeping motion. However, such equations are not always easily solved, especially for complex geometries or when there are many particles in suspension. Moreover, they are based on the hypothesis that the solvent is a continuum. But in conditions relevant for microfluidic devices, this hypothesis is not always fulfilled and fluctuations of the solvent velocities may be relevant. To study diffusion of colloids in microcavities it is therefore important to test different tools, such as simulations in which the solvent is explicitly introduced, or in which the solvent velocity is allowed to fluctuate. In this work, we use the multiparticle collision dynamics (MPCD) technique, initially proposed by Malevanets and Kapral.[18] It consists of a coarse-grained model to describe the solvent completed with specific rules (see below) to describe solvent-solute interactions. It has been successfully used to study hydrodynamic interactions in complex fluids, at equilibrium and far from it. For a review, see Ref. 19.

We will briefly introduce the simulation technique in Sec. II. In Sec. III, we discuss the measurements of friction and diffusivity. In Sec. IV, we will analyze the simulations results for the diffusion of a spherical particle inside a microcavity in the shape of a closed cylinder. We will show that the friction is different along the radial, azimuthal, and axial directions, and that the corresponding diffusion coefficients change in different ways with the particle's radial and axial position. In Sec. V, we will compare our results with

a)Electronic mail: a.imperio@virgilio.it.
b)Electronic mail: j.t.padding@gmail.com.
c)http://cbp.tnw.utwente.nl.

experimental and theoretical data. A simplified model to interpret our results is given in Sec. VI. Finally, we give our conclusions in Sec. VII.

II. SIMULATION TECHNIQUE

A severe difficulty in simulating colloidal solutions is to correctly deal with the large range of time and length scales involved. Whereas the solvent velocities generally relax in less than a picosecond, colloids typically diffuse over a length equal to their own size in seconds. Fortunately, it is often not necessary to exactly reproduce such time and length scales. A coarse-grained approach is possible in which the scales are telescoped together,[20] while keeping an order of magnitude difference between each relevant time scale.

As already mentioned, we will use multiparticle collision dynamics (Refs. 18 and 19) to describe the solvent degrees of freedom, with no-slip boundary conditions for the solvent–solute interactions. The implementation of the no-slip boundary conditions has been discussed in detail in Ref. 21. The dynamics of the system is made up of two steps: streaming and collision. In the streaming step, the position and velocity of each particle is propagated for a time δt by solving Newton's equations of motion. During the collision a lattice is placed in the system.[22] This lattice is typically cubic, with a lattice constant a. Solvent particles are then attributed to the cells in which they happen to be positioned. Next the velocities $\mathbf{v}_i$ of all particles are stochastically rotated, relative to the center of mass of the corresponding cells according to the formula

$$\mathbf{v}_i'(t) = \mathbf{u} + \boldsymbol{\Omega}\{\mathbf{v}_i(t) - \mathbf{u}\}, \tag{1}$$

where $\mathbf{u}$ is the mean velocity of the particles within the collision cell to which particle i belongs and $\boldsymbol{\Omega}$ is a matrix which rotates velocities by a fixed angle α around a randomly oriented axis. Through the stochastic rotation of the velocities, the solvent particles can effectively exchange momentum without the need of introducing direct forces between them. As the collision step preserves mass, linear momentum and energy, the correct hydrodynamic behavior is obtained on the mesoscopic scale.[18,23]

When colloids are present, Newton's equations of motion are solved also for them during the streaming step. However, special care must be taken when no-slip boundary conditions are applied on the colloidal surface and on the confining walls. The implementation of the no-slip boundary conditions is described in the following.

Streaming step: when a solvent particle crosses the colloid (or wall) surface, it is moved back to the impact position. Then a new velocity is extracted from the following distributions for the tangent (v_t) and the normal component (v_n) of the velocity, with respect to the surface velocity

$$p(v_n) = \frac{m v_n}{k_B T} \exp\left(-\frac{m v_n^2}{2 k_B T}\right), \tag{2}$$

$$p(v_t) = \sqrt{\frac{m}{2\pi k_B T}} \exp\left(-\frac{m v_t^2}{2 k_B T}\right). \tag{3}$$

Here m is the mass of the solvent particle, k_B is the Boltzmann's constant, and T is the temperature of the system. Once the velocity has been updated, the particle is displaced for the remaining part of the integration time step.

Collision step: virtual particles (VPs) are inserted in those parts of the collision cells which are physically occupied by the colloid or by the container walls. The VP density matches that of the MPCD solvent, while their velocities $\mathbf{v}_i^{\mathrm{VP}}$ are obtained from a Maxwell–Boltzmann distribution, whose average velocity is equal to the local velocity of the colloid or to the velocity of the walls, and the temperature is the same as in the solvent. Notice that we do not take rotations of the particles into account. VPs are sorted into the collision cells according to their coordinates, exactly as the MPCD particles. This method is similar to that used in Refs. 24–27. Then the average velocity of the center of mass of the cell is computed as

$$\mathbf{u} = \frac{\sum_{i=1}^{n_{\mathrm{MPCD}}} \mathbf{v}_i(t) + \sum_{i=1}^{n_{\mathrm{VP}}} \mathbf{v}_i^{\mathrm{VP}}(t)}{n_{\mathrm{MPCD}} + n_{\mathrm{VP}}}, \tag{4}$$

where n_{MPCD} and n_{VP} are the number of MPCD particles and VPs, respectively, belonging to the same cell. Velocities of both MPCD and VP belonging to the same cell are rotated according to the rule given in Eq. (1).

Due to the exchange of momentum between the solvent and the colloidal particle, the force exerted upon the latter can be expressed as $\mathbf{F} = \mathbf{f_s} + \mathbf{f_c}$, where $\mathbf{f_s}$ and $\mathbf{f_c}$ are the forces during the streaming and the collision step, respectively. The former can be calculated as

$$\mathbf{f_s} = -\frac{1}{\delta t} \sum_{i=1}^{Q} \Delta \mathbf{p}_i, \tag{5}$$

where Q is the number of MPCD particles which have crossed the surface of the colloid between two collision steps, and $\Delta \mathbf{p}_i = m \Delta \mathbf{v}_i$ is the change in momentum of solvent particle i, which has been scattered by the colloid. The force exerted during the collision step is

$$\mathbf{f_c} = \frac{1}{\delta t} \sum_{i=1}^{q} \Delta \mathbf{p}_i^{\mathrm{VP}}, \tag{6}$$

where q is the total number of virtual particles which belong to a tagged colloid, and $\Delta \mathbf{p}_i^{\mathrm{VP}}$ is the change in momentum of the virtual particle i as a consequence of the collision step.

The force exerted by the solvent on the colloidal particle, will be used in Sec. IV in order to measure the friction on the particle itself.

In our simulations, we use a collision angle $\alpha = \pi/2$, an average solvent particle density of five particles per collision cell, and a collision time step $\delta t = 0.1 t_0$, where $t_0 = a\sqrt{m/k_B T}$ is the simulation unit of time. This choice leads to a mean free path which is an order of magnitude smaller than the collision cell size a, which is important to simulate the dynamics of a colloid in a liquid instead of a gas.[20] Simulations have been performed with a colloidal sphere of radius $R_{\mathrm{col}} = 3a$, which is sufficiently large to accurately resolve the hydrodynamic field to distances as small as $R_{\mathrm{col}}/6$, as already shown in Refs. 20 and 28. The radius and height of the closed cylinder are $R_{\mathrm{cyl}} = H_{\mathrm{cyl}} = 54a$. In this way we can make a

direct comparison with the experimental case discussed in Ref. 17. The typical length of a simulation run is about 1.5×10^6 integration time steps.

III. MEASURING FRICTION AND DIFFUSIVITY

The drag force $\mathbf{F}$ and torque $\mathbf{T}$ acting on a particle that moves through a fluid with a steady velocity $\mathbf{V}$ and steady angular velocity $\mathbf{\Omega}$ can be expressed as

$$-\begin{pmatrix}\mathbf{F}\\ \mathbf{T}\end{pmatrix} = \mathbf{M}\begin{pmatrix}\mathbf{V}\\ \Omega\end{pmatrix}, \tag{7}$$

where $\mathbf{M}$ is the friction tensor represented by a 6×6 matrix. The friction matrix can be subdivided in four blocks:

$$\mathbf{M} = \begin{pmatrix}\Xi^t & \Xi^{tr}\\ \Xi^{rt} & \Xi^r\end{pmatrix}, \tag{8}$$

where the superscript t stands for translation, r stands for rotation, and tr and rt stand for the coupling between rotational motion and (translational) force and between translational motion and (rotational) torque, respectively. The blocks of the matrix $\mathbf{M}$ can be obtained in the following manner. During the simulation the colloidal sphere is kept in a fixed position and fixed orientation by applying an external constraint force $\mathbf{F}^c$ and external constraint torque $\mathbf{T}^c$. The constraint force and torque are equal, but opposite to the total force and torque exerted by the solvent on the sphere $\mathbf{F}^c = -\mathbf{F}$ and $\mathbf{T}^c = -\mathbf{T}$. Through the fluctuation–dissipation theorem and the autocorrelation functions of $\mathbf{F}^c$ and $\mathbf{T}^c$ can be connected to each of the components of the friction tensor. For example, the explicit expression for Ξ^t (Refs. 28 and 29) is

$$\Xi^t_{\alpha\beta} = \frac{1}{k_B T}\int_0^\infty \mathrm{d}\tau \left\langle F^c_\alpha(\tau_0+\tau)F^c_\beta(\tau_0)\right\rangle_{\tau_0}. \tag{9}$$

Similarly, we can also measure

$$\Xi^{tr}_{\alpha\beta} = \frac{1}{k_B T}\int_0^\infty \mathrm{d}\tau \left\langle F^c_\alpha(\tau_0+\tau)T^c_\beta(\tau_0)\right\rangle_{\tau_0} \tag{10}$$

and so on. The quantities α, β refer to two of the cylindrical coordinates r, θ, z and the average is taken over many different time origins τ_0. As shown in Fig. (1), for a given position of the sphere we can define an orthogonal frame with unit vectors pointing in the local r, θ, and z directions. Because the sphere is in a fixed position, this orthogonal frame does not change during the simulations.

The friction tensor $\mathbf{M}$ is connected to the diffusion tensor through the Einstein relation $\mathbf{D} = k_B T \mathbf{M}^{-1}$. The diffusion tensor can be subdivided in blocks too:

$$\mathbf{D} = \begin{pmatrix}D^t & D^{tr}\\ D^{rt} & D^r\end{pmatrix}, \tag{11}$$

where D^t is the translational diffusion tensor, D^r is the rotational diffusion tensor, and D^{tr} and D^{rt} are determine the amount of cross correlation between translational and rotational displacements.

A strong coupling between translation and rotation is expected when the particle gets very close to a wall. This will cause a torque-free particle to rotate when it is translated along the wall, and vice versa a force-free particle to translate when it is rotated near a wall. However, after a preliminary analysis on the walls' effects, based upon a sphere nearby a flat wall[7] and inside an infinitely long cylinder,[8] for the particular gaps we are interested in, we find that such a coupling is very small: in the worst case scenario ($d/R = 0.5$) the effect of including translation–rotation coupling on the translational diffusion is less than 2%. We expect that the contribution due to the coupling between rotation and translation is small in the closed cylinder as well, so that we can neglect the terms Ξ^{tr} and Ξ^{rt} in the friction tensor.

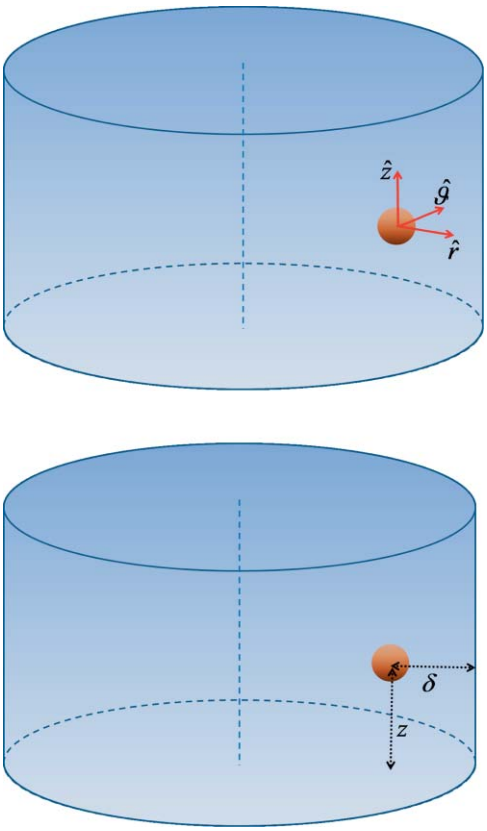

FIG. 1. For a generic sphere position, we plot the unit vectors of the radial ($\hat{r}$), azimuthal ($\hat{\theta}$), and axial ($\hat{z}$) directions. The distance from the cylindrical walls is δ, while the distance from the bottom wall is z. When the sphere is in the midplane $z = H_{\mathrm{cyl}}/2$, when the sphere is placed along the axis $\delta = R_{\mathrm{cyl}}$.

In this paper, we focus on two cases: one in which the particle is set in the midplane of the cylinder and another in which it is located along its axis. For both these cases, symmetry requires that Ξ^t is diagonal. Therefore, the translational diffusion tensor D^t is also diagonal and, under the hypothesis that the coupling between rotation and translation is negligible, we set $D^t_{rr} = k_B T/\Xi^t_{rr}$, $D^t_{\theta\theta} = k_B T/\Xi^t_{\theta\theta}$ and $D^t_z = k_B T/\Xi^t_{zz}$.

Because in this paper we measure only the translational diffusion and not the rotational diffusion, we drop the superscript t and simplify the notation as D_r, D_θ, and D_z. Some specific components of the running integral of the autocorrelation function of $\mathbf{F}^c$ are shown in Fig. 2: the sphere is in the midplane but at different distances δ from the cylindrical walls. In particular, in the upper panel we show the radial component of the friction Ξ_{rr}, while in the bottom panel the azimuthal one $\Xi_{\theta\theta}$.

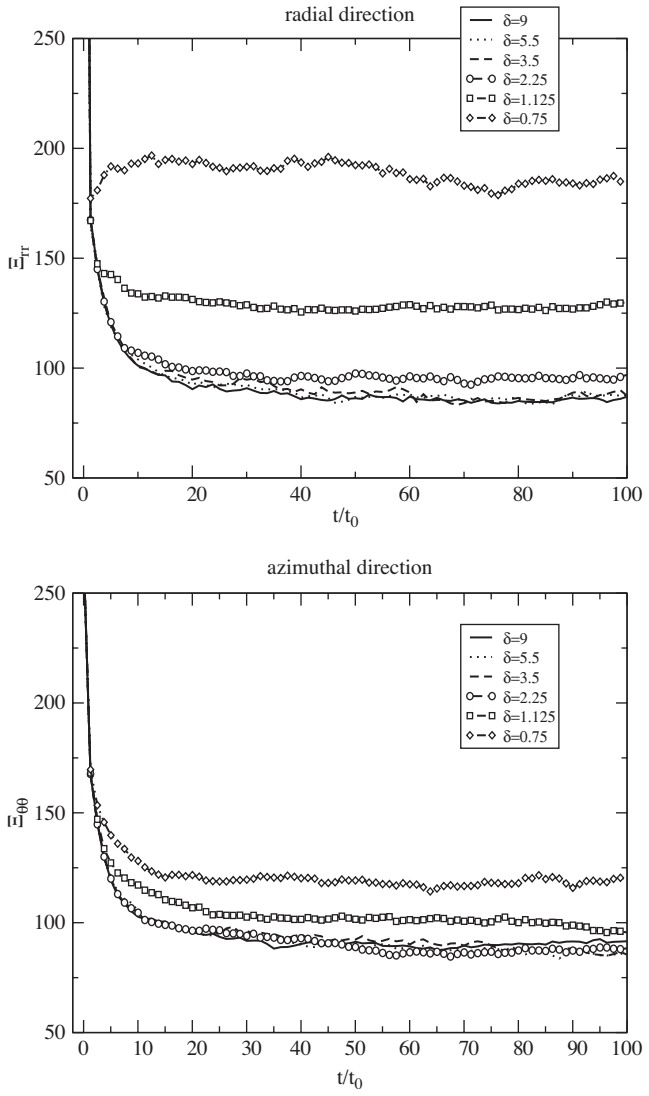

FIG. 2. Running integral of the autocorrelation function of the constraint force F^c applied to the sphere in the midplane. The distance δ from the cylindrical wall is in units of the particle diameter. Time is in units of $t_0 = a(m/k_BT)^{1/2}$ and friction in units of m/t_0. (Upper panel) Radial friction. (Bottom panel) Azimuthal friction, which is very similar to the axial friction (not shown in this picture).

Finally, we note a peculiarity which is linked to the fact that in our simulations a colloidal particle collides with only a few solvent particles within each particular time step δt. If we consider a particular direction α, there are essentially two contributions to the total friction: one coming from the local Brownian collisions with the particles of the fluid (ξ^B), while the other is due to the long-range hydrodynamic interactions (flow fields) (ξ^H). A simple empirical formula says that the hydrodynamic and the Brownian friction should be added in parallel[30,31] in order to obtain the total friction

$$\frac{1}{\Xi_{\alpha\alpha}} = \frac{1}{\xi^B} + \frac{1}{\xi^H_{\alpha\alpha}}, \tag{12}$$

where ξ^B does not depend on the sphere's position and corresponds to the height of the short-time peak of the integral in Eq. (9); its value is 645 ± 1 (in units m/t_0) for all diagonal components. The long-time limit of the profiles shown in Fig. 2 provides the total friction upon the sphere. Thus, the hydrodynamic term can be extracted by inverting Eq. (12). For validation of this method and further applications of this concept see Refs. 20 and 28.

IV. SIMULATION RESULTS

The measured diffusion coefficients are summarized in Fig. 3 for the midplane (upper panel) and for the cylinder axis (bottom panel). The diffusion is normalized to the bulk value D_0 for a sphere with no-slip boundary conditions upon its surface. The latter is provided by the Stokes–Einstein law: $D_0 = k_BT/(6\pi\nu R_{\rm col})$, where ν is the solvent viscosity.

First, we focus on the case where the sphere is located in the midplane of the cavity. When the colloidal sphere is

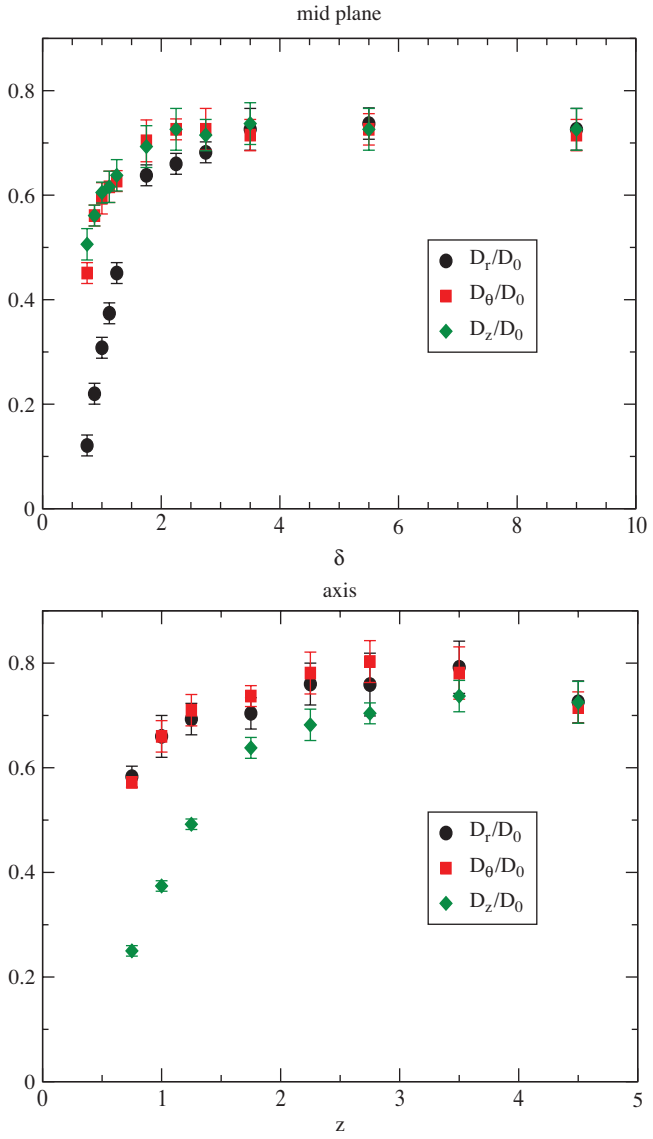

FIG. 3. Diffusion coefficients along the radial ($\hat{r}$), azimuthal ($\hat{\theta}$), and axial ($\hat{z}$) direction. (Upper panel) The sphere is in the midplane and δ is the separation from the cylindrical walls. (Bottom panel) The sphere is placed along the cylinder axis and z is the distance from the closest end wall. Distances are in units of the particle diameter. Diffusion is in units of the bulk value D_0 (see main text).

set near the center of this midplane (large δ), we expect that $D_r = D_\theta$ because of symmetry. Actually, we observe that all three diagonal components are almost the same and their value is significantly lower (25%) than in a bulk system. When the sphere is shifted toward the cylindrical wall, the diffusion decreases even more. For off-centered positions, the radial component D_r decreases more rapidly than D_θ and D_z do.

Next, we focus on the case where the sphere is located on the central axis of the cavity, at a distance z from the nearest end wall. Although in this case technically no azimuthal direction can be defined, we have made two orthogonal measurements perpendicular to the z axis, and labeled them as D_r and D_θ in the bottom panel of Fig. 3. As expected, because of symmetry we find $D_r = D_\theta$ within uncertainties. Close to the end wall, D_z decreases much faster than the other two components do. This situation is similar to the case of a sphere close to a flat wall. However, the similarity is only qualitative and not quantitative, as we will discuss in Sec. VI.

V. COMPARISON WITH EXPERIMENTAL AND THEORETICAL PREDICTIONS FOR THE CLOSED CYLINDER

First, we compare our data with some theoretical results published recently and next with some recent experimental results. It is interesting to notice that our results presented in the upper panel of Fig. 3 are in agreement with the findings in Bhattacharya *et al.*[13] where hydrodynamic calculations are performed of the drag on a particle in an infinitely long cylinder. In particular, the authors observe that for $R_{\rm cyl} \geq 4R_{\rm col}$, all three diagonal components of the friction increase monotonically when the particle approaches the wall. The radial friction is expected to vary stronger than the other two frictions, because its motion is perpendicular to the confining walls, while in the other cases the motion is tangent to the wall. As discussed in Ref. 13, the resistance for the radial motion is inversely proportional to the gap between particle and wall, while for the tangential motions it varies logarithmically with the gap. Qualitatively our results are similar, in the sense that the azimuthal diffusion for small particle–wall separations varies slower than the radial diffusion does; this suggests that the role of the cylindrical wall is dominant in this region. However, we will show that for our squat cylinder the role of the end walls cannot be neglected at any sphere position (Sec. VI).

We have performed two additional simulations in order to compare the results with the theoretical predictions in Ref. 16 for the axial friction $\gamma_z = \xi_z/\xi_0$ in a closed cylinder. Here $\xi_0 = 6\pi\nu R_{\rm col}$ corresponds to the friction on a sphere in an unbounded system. The two cases that we have chosen are, one in which the cylinder is very narrow and long, and one in which it is squat. The results are summarized in Table I. The agreement is good.

In case the closed cylinder is very long, the friction on a sphere in the midplane should not be very different from that predicted for a sphere in an infinitely long tube. For example, for the case $R_{\rm cyl} = 4R_{\rm col}$ the friction inside an infinitely long cylinder can be found in Ref. 13. In particular for a sphere placed on the cylinder axis, the values are: $\gamma_r = 1.763$ and $\gamma_z = 1.992$. Our simulation results for a closed cylinder with the same radius but finite length $H_{\rm cyl} = 20R_{\rm col}$ agree within error bars: $\gamma_r = 1.79 \pm 0.07$ and $\gamma_z = 2.03 \pm 0.08$. We can conclude that for a long cylinder the role of the end walls is minimal.

TABLE I. Axial friction upon a sphere in a closed cylinder. The radius and the height of the cylinder are in units of the sphere radius. Theoretical predictions corresponds to (Ref. 16). The friction is normalized to the bulk value which is $\xi_0 = 6\pi\nu R_{\rm col}$.

$R_{\rm cyl}$	$H_{\rm cyl}$	Lecoq 2007	Simulation
4	20	1.979	2.03 ± 0.08
10.7	6	1.843	1.82 ± 0.07

The dependence of the diffusion on the spatial position of a particle inside a closed cylinder has been recently studied through experiments in Ref. 17. The authors discuss the case of a micrometer-size particle in an aqueous suspension. The microcavity is produced via soft lithography where PDMS membranes are used. In Fig. 4, we compare their experimental results (open symbols) with our simulation results (filled symbols) in the midplane for the radial and the azimuthal components. The setup of the experiments did not allow the measurement of the axial diffusion. The agreement between the two sets of data is good. In particular, the region where D_r and D_θ begin to differ is well captured.

The good agreement with both experimental and theoretical predictions reaffirms that MPCD simulations enable us to predict quantitatively the friction on a colloidal particle in a confined space.

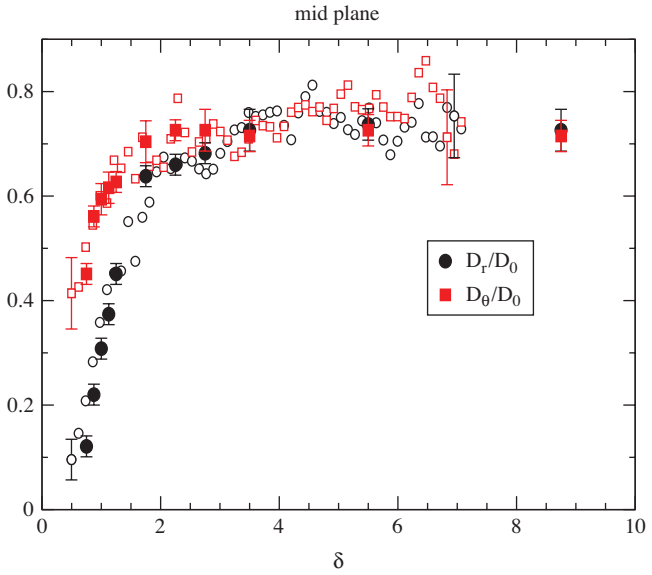

FIG. 4. A comparison between simulation results (filled symbols) and experimental data (see Ref. 17) (open symbols) for the diffusion coefficient in the midplane of a closed cylinder. Radial diffusion (circles). Azimuthal diffusion (squares). The wall–particle distance δ is in units of the particle diameter d. $R_{\rm cyl} = 9d$ and $H_{\rm cyl} = 9d$. For the sake of clarity, we show the error bars for only a few experimental data points.

VI. DISCUSSION OF WALL EFFECTS

We will now discuss the effects of confinement on the diffusivity of a colloidal particle, by focussing on the effects of each individual type of boundary, i.e., cylinder or flat wall.

Generally speaking, for small Reynolds numbers, the correction term to the friction on a confined particle is $\gamma = \xi/\xi_0$, where ξ_0 is the friction on a sphere in an unbounded solvent. In principle, γ depend on the direction of motion. Since there are no sufficiently general solutions available of the Navier–Stokes equations for a closed cylinder, we will try to estimate the total wall corrective factor as a combination of the corrective terms due to simplified geometries, such as the infinitely long cylinder, flat walls, and square ducts. For ease of reference we reproduce explicit formulas available in the literature.

The wall correction for the axial friction on a sphere at an eccentric position is, approximately,[5]

$$\gamma_z^{\mathrm{cyl}} = 1 + \left(2.10444 - 0.6977\left(\frac{R_{\mathrm{cyl}} - \delta}{R_{\mathrm{cyl}}}\right)^2\right)\left(\frac{R_{\mathrm{col}}}{R_{\mathrm{cyl}}}\right). \tag{13}$$

This expression is valid mainly near the axis of the cylinder. If the sphere is exactly on the axis, a more precise correction due to Bohlin,[32] also reported in Ref. 5, is

$$\gamma_z^{\mathrm{cyl}} = \left[1 - 2.10444\chi + 2.08877\chi^3 - 6.94813\chi^5 + \right. \\ \left. -1.372\chi^6 + 3.87\chi^8 - 4.19\chi^{10}\right]^{-1}, \tag{14}$$

where $\chi = R_{\mathrm{col}}/R_{\mathrm{cyl}}$. When the sphere is small (relative to the cylinder's diameter) and very close to the cylinder wall, it is expected that the curvature of the wall is not very important and that the sphere behaves like near to a flat wall.[33] In such a case the wall correction for the parallel motion is[5]

$$\gamma_{||}^{\mathrm{wall}} = \left[1 - \frac{9}{16}\left(\frac{R_{\mathrm{col}}}{h}\right) + \frac{1}{8}\left(\frac{R_{\mathrm{col}}}{h}\right)^3 + \right. \\ \left. -\frac{45}{256}\left(\frac{R_{\mathrm{col}}}{h}\right)^4 - \frac{1}{6}\left(\frac{R_{\mathrm{col}}}{h}\right)^5\right]^{-1}, \tag{15}$$

while for the perpendicular motion it is

$$\gamma_{\perp}^{\mathrm{wall}} = \frac{4}{3}\sinh(\alpha)\sum_{n=1}^{\infty}\frac{n(n+1}{(2n-1)(2n+3)} \times \\ \left[\frac{2\sinh(2n+1)\alpha + (2n+1)\sinh 2\alpha}{4\sinh^2(n+0.5)\alpha - (2n+1)^2\sinh^2(\alpha)} - 1\right]. \tag{16}$$

Here $\alpha = \cosh^{-1}(h/R_{\mathrm{col}})$, in which h is the distance of the sphere from the wall.

In Fig. 5 we plot the simulation data for D_z and the theoretical predictions for an infinitely long cylinder. We use Eq. (13) which is valid near the cylinder axis (dashed line) and Eq. (15) which is valid near the the cylinder walls (solid line). The profile provided for the region nearby the cylindrical wall is also in good agreement with the model in Ref. 8. Although such equations have only a limited range of validity, in Fig. 5 they have been plotted along the entire range of distances we are interested in. In the same picture we also

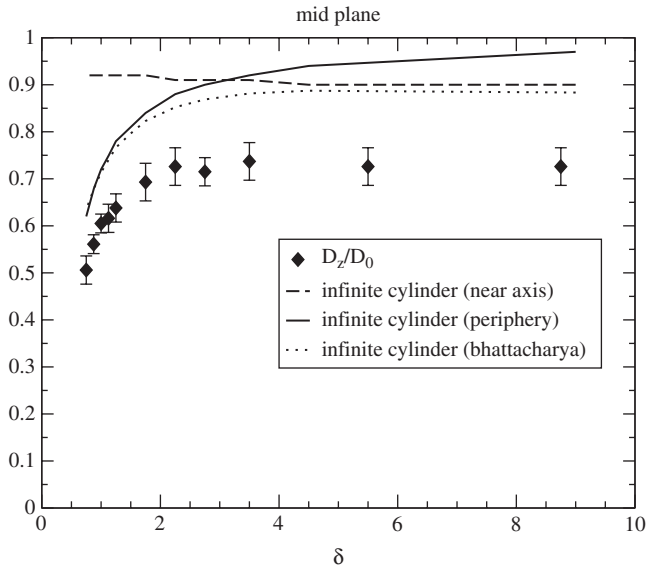

FIG. 5. Axial diffusion coefficient in the midplane. Simulations (diamond symbols) are compared with: (i) prediction for an infinitely long cylinder, valid near the axis (dashed line), (ii) predictions for a flat wall, valid at the periphery of the cylinder (solid line), and (iii) predictions from numerical solutions of the Navier–Stokes equations in an infinitely long cylinder (dotted line). All these predictions disregard the role of the end walls, so that the diffusion is globally overestimated relative to our simulation results.

show the diffusion obtained from the numerical solution of the Navier–Stokes equations (dotted line) for a cylinder provided by S. Bhattacharya (private communication), according to the method described in Ref. 13. We see that the latter result agrees very well with Eqs. (13) and (15) in the appropriate limits. The discrepancy with our simulation results, however, is quite large for all values of δ. This comparison clearly shows that the end walls' effects are important for all particle positions in the midplane of the cylinder both close to the axis, as well as in proximity of the cylinder walls, in case the separation between the end walls is of the order of the cylinder diameter or less.

In the following, we will attempt to find a simple model that can predict the combined effects of all walls, at least with the dimensions of our simulation box.

It has been shown[34] that when the particle is placed on the axis of a container and the size of the particle is small compared to the width of the container, the axial friction depends only weakly on the precise geometry, whether cylindrical or rectangular. Inspired by this observation, we approximate the closed cylinder by a rectangular parallelepiped circumscribed to it, as shown in Fig. 6.

We then express the total correction factor Γ for the friction as a combination of single flat-wall corrections γ:

$$\Gamma = \gamma_1(d_1) + \gamma_{1'}(d_{1'}) + \gamma_2(d_2) + \gamma_{2'}(d_{2'}) \\ +\gamma_3(d_3) + \gamma_{3'}(d_{3'}) - (n-1), \tag{17}$$

where d_i refers to the distance of the particle from flat wall i, as numbered in Fig. 6, n is the number of boundaries or walls included in the model. In the parallelepiped model, $n = 6$. We have to subtract $n - 1$ in order to avoid overcounting the bulk

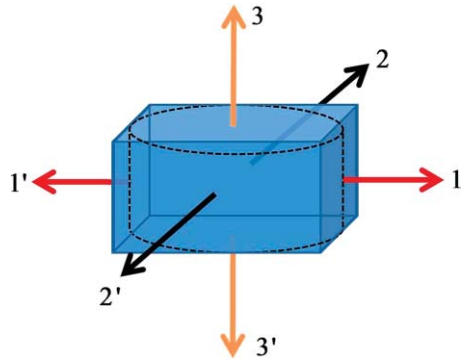

FIG. 6. Rectangular parallelepiped circumscribing the cylinder. For a generic particle position, the indexes 1 and 1′ refer to the walls perpendicular to the radial motion; 2 and 2′ to the walls perpendicular to the azimuthal motion; and 3 and 3′ for the walls perpendicular to the axial motion.

value; this is a mere consequence of the definition of the wall correction factor.

Before continuing with the closed cylinder, let us consider how our model performs for infinitely long systems, in particular for an infinitely long cylinder and for an infinitely long square duct. Our model in this case has just for flat walls, since we must remove the walls 3 and 3′ in Fig. 6; consequently $n = 4$ in this case. For the cylinder we have $\gamma_{\text{axis}} = 1.132$, when $R_{\text{cyl}} = 18R_{\text{col}}$; for the square duct we have $\gamma_{\text{sd}} = 1.118$ when the half width of the square is equal to $18R_{\text{col}}$ (Ref. 34) and for our model we find $\Gamma = 1.129$. All three numbers agree reasonably well.

Coming back to the case of the closed cavity, the motion along the radial direction can be decomposed into a motion perpendicular to two walls and parallel with respect to the remaining four walls. Similar conclusions can be drawn for the azimuthal and axial motion. So we can specialize the relation in Eq. (17) in the following manner:

$$\Gamma_r = \gamma_{\perp,1}(d_1) + \gamma_{\perp,1'}(d_{1'}) + \gamma_{||,2}(d_2) + \gamma_{||,2'}(d_{2'}) + \gamma_{||,3}(d_3) + \gamma_{||,3'}(d_{3'}) - 5, \tag{18}$$

$$\Gamma_\theta = \gamma_{||,1}(d_1) + \gamma_{||,1'}(d_{1'}) + \gamma_{\perp,2}(d_2) + \gamma_{\perp,2'}(d_{2'}) + \gamma_{||,3}(d_3) + \gamma_{||,3'}(d_{3'}) - 5, \tag{19}$$

$$\Gamma_z = \gamma_{||,1}(d_1) + \gamma_{||,1'}(d_{1'}) + \gamma_{||,2}(d_2) + \gamma_{||,2'}(d_{2'}) + \gamma_{\perp,3}(d_3) + \gamma_{\perp,3'}(d_{3'}) - 5, \tag{20}$$

where the expression for the parallel (||) and perpendicular (⊥) corrections are given by Eqs. (15) and (16), respectively. In Fig. 7, we compare these predictions with our simulation results; the upper panel refers to the midplane, while the bottom panel to the particle placed along the container axis. The agreement is very good, which is rather surprising given the simplicity of the model. Note, however, that the radial and azimuthal diffusion coefficients predicted by our model are not exactly equal on the axis, as they should be.

Its success is possibly caused by a subtle cancellation of errors, which we will discuss next.

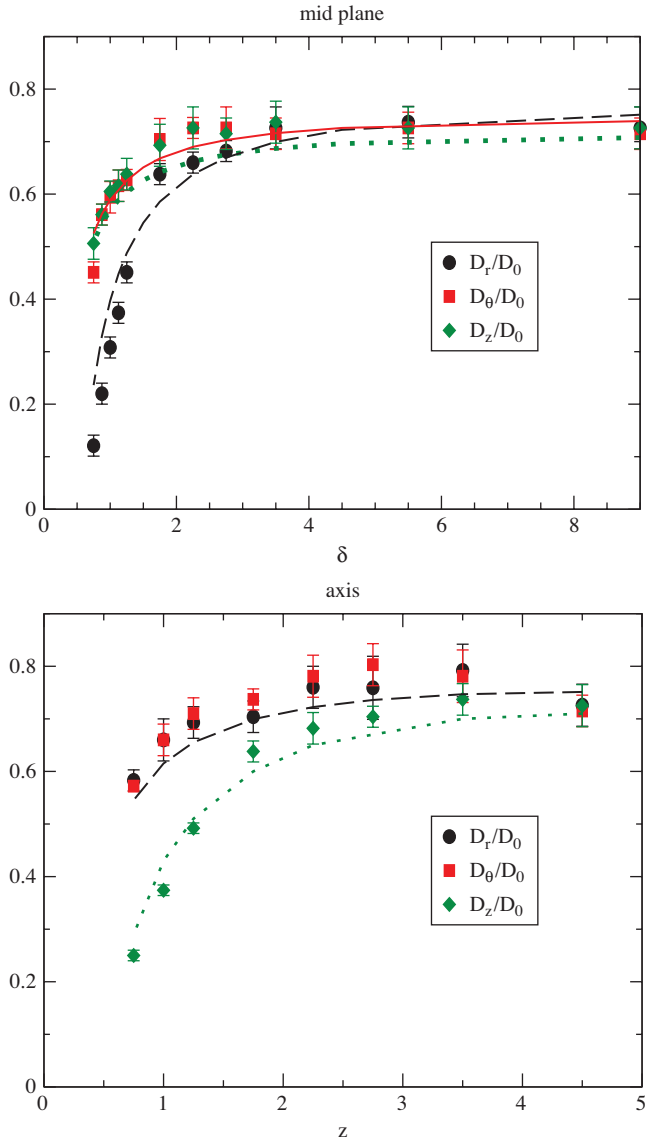

FIG. 7. (Upper panel) Diffusion in the midplane, where δ is the distance from the cylinder wall. (Bottom panel) Diffusion along the axis, where z is the distance from the bottom wall. Symbols are for simulation data. Lines for the rectangular parallelepiped model: D_r (dashed line), D_θ (solid line), D_z (dotted line).

The rectangular parallelepiped model is based upon a linear superposition of the walls' effects. In this approximation, we disregard the influence of the curvature of the vertical walls and that of the corners obtained by the intersection of the cylindrical wall and the top and bottom walls. For a particle in the midplane and close to the vertical wall, ignoring the effect of the curvature, the presence of the corners obtained by the intersection of the cylindrical wall and the top and bottom walls leads to larger frictions, so that their neglect leads to an underestimation of the friction and consequently to an overestimation of the diffusion coefficients.

On the other hand, using the superposition model for the top and bottom walls per se leads to a slight overestimation of the perpendicular frictions and thus to slight underestimations of the corresponding diffusions. For the slit geometry this may be seen in Fig. 4 in Ref. 35. The magnitude of such effects

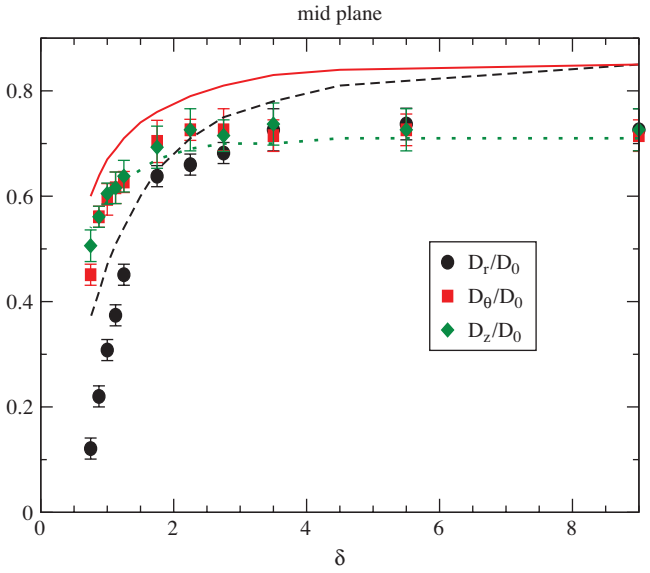

FIG. 8. Comparison between simulation data and the superposition model applied to a combination of an infinitely long cylinder and two flat walls. Symbols are for simulation data. Lines for the rectangular parallelepiped model: D_r (dashed line), D_θ (solid line), D_z (dotted line).

depends on the distance of the particle from the walls. For the present case, the parallel friction for a slit geometry is quite well represented by the linear superposition model, whereas the perpendicular friction is overestimated.

For the configurations studied here the overestimation of the friction perpendicular to the end walls is large enough to compensate the underestimation of the total friction which is intrinsic to the superposition model applied to a geometry with corners.

The above discussion can also be cast in the framework of the method of reflections, where the role of walls is mimicked through a set of images of the colloidal particle. This set of images is used to enforce a zero velocity boundary condition for the fluid near the planar surfaces. For a real parallelepiped, the superposition model only takes into account the six images due to the single reflections on each of the sides of the parallelepiped. However, every time a new image is introduced (to treat a new wall) the fluid velocity profile on the existing walls is modified. This is then corrected, usually in an iterative fashion. Corner effects arise from the reflection of each image particle with respect to two perpendicular walls. In the slit geometry, instead, successive corrections to the linear superposition, comes from the multiple reflections of the images, similarly to those that appear in a barber shop.

We have also tried a superposition of the friction expressions for an infinitely long cylinder (private communication from Bhattacharya) and two planar walls. In this case, the agreement with the simulation data is less good, especially for the radial and azimuthal diffusion as shown in Fig. 8.

This result shows that the superposition model is quite sensitive to the details of the surfaces we apply it, and therefore it should be applied with care.

VII. CONCLUSIONS

We have studied, by means of particle-based simulations, the diffusion of a spherical particle inside a microcavity in the shape of a squat closed cylinder. We have analyzed the diffusion in the middle plane as a function of the particle–cylinder separation δ and along the axis of the cylinder as a function of the particle-end wall separation z. For our squat cylinder we find that when the sphere is near the center of the cylinder, the diffusion is the same along the radial, azimuthal, and axial direction and it is significantly lower than in the bulk. In the midplane, when the particle is shifted toward the cylinder wall, the diffusion decreases more in the radial direction than in the azimuthal and axial ones. The last two are very similar to each other. When the particle is shifted along the axis we find that the diffusion decreases much more along the axial direction than perpendicular to it. In general, we can say that the diffusion in the direction mostly parallel to the closest confining wall, decreases slower than in the direction perpendicular to it.

We have compared our simulations with experimental results for a micrometer-sized particle in a cylindrical microcavity, finding good agreement. We also find good agreement with the theoretical predictions for a closed cylinder reported in Ref. 16.

Finally, we have shown that the simplest approximation to capture confinement effects, namely, one which uses the result for an infinitely long cylinder for the axial diffusion, does not work. Neither does treating the closest wall nor does a flat wall when the particle is at the periphery of the box. The end wall effects appear very important for all positions of the sphere inside the squat cylinder. We have investigated a simplified model in which the effect of all walls is approximated as a superposition of the effects of individual walls of a rectangular parallelepiped circumscribing the cylinder. This model works well for diffusion coefficients both in the midplane and along the axis, but it owes its success to a fortunate cancellation of errors.

ACKNOWLEDGMENTS

We thank Sukalyan Bhattacharya for fruitful discussions, suggestions, and kindly providing the numerical data to compare and validate our simulation results.

[1]K. van Ommering, C. C. H. Lamers, J. H. Nieuwenhuis, C. L. J. van Ijzendoorn, and M. W.J. Prins, J. Appl. Phys. **105**, 104905 (2009).
[2]K. van Ommering, J. H. Nieuwenhuis, C. L. J. van Ijzendoorn, L. J. Koopmans, and M. W. J. Prins, Appl. Phys. Lett. **89**, 142511 (2006).
[3]T. M. Squires, R. J. Messinger, and S. R. Manalis, Nat. Biotechnol. **26**, 417 (2008).
[4]I. Shestopalov, J. D. Tice, and R. F. Ismagilov, Lab Chip **4**, 316 (2004).
[5]J. Happel and H. Brenner, *Low Reynolds Number Hydrodynamics*, Prentice-Hall International Series in the Physical and Chemical Engineering Sciences (1996).
[6]S. Kim and S. J. Karrila, *Microhydrodynamics: Principles and Selected Applications* (Butterworth-Heinemann, Boston, 1991).
[7]A. J. Goldman, R. G. Cox, and H. Brenner, Chem. Eng. Sci. **22**, 637 (1967).
[8]A. Falade and H. Brenner, J. Fluid Mech. **193**, 533 (1988).
[9]B. R. Hirschfeld, H. Brenner, and A. Falade, PCH, PhysicoChem. Hydrodyn. **5**, 99 (1985).
[10]R. G. Cox and H. Brenner, J. Fluid Mech. **28**, 391 (1966).

[11]R. M. Sonshine, R. G. Cox, and H. Brenner, Appl. Sci. Res. **16**, 273 (1966).
[12]E. R. Lindgren, Phys. Scr. **60**, 97 (1999).
[13]S. Bhattacharya, C. Mishra, and S. Bhattacharya, J. Fluid Mech. **642**, 295 (2010).
[14]J. R. Blake, J. Fluid Mech. **95**, 209 (1979).
[15]O. Sano, J. Phys. Soc. Jpn. **56**, 2713 (1987).
[16]N. Lecoq, K. Masmoudi, R. Anthore, and F. Feuillebois, J. Fluid Mech. **585**, 127 (2007).
[17]H. B. Eral, J. M. Oh, D. van den Ende, F. Mugele, and M. H. G. Duits, Langmuir **26**, 16722 (2010).
[18]A. Malevanets and R. Kapral, J. Chem. Phys. **110**, 865 (1999).
[19]G. Gompper *et al.*, Adv. Polym. Sci. **221**, 1 (2009).
[20]J. T. Padding and A. A. Louis, Phys. Rev. E **74**, 031402 (2006).
[21]A. Imperio, J. T. Padding, and W. J. Briels, "Force calculation on walls and embedded particles in multiparticle collision dynamics simulations," Phys. Rev. E (to be published); e-print arXiv:cond-mat/1102.2827.
[22]T. Ihle and D. Kroll, Phys. Rev. E **63**, 020201(R) (2001).
[23]A. Malevanets and R. Kapral, J. Chem. Phys. **112**, 7260 (2000).
[24]A. Lamura, G. Gompper, T. Ihle, and D. M. Kroll, Europhys. Lett. **56**, 319 (2001).
[25]R. G. Winkler and C. C. Huang, J. Chem. Phys **130**, 074907 (2009).
[26]J. O. Gotze, H. Noguchi, and G. Gompper, Phys. Rev. E **76**, 046705 (2007).
[27]M. T. Dountown and H. Stark, J. Phys.: Condens. Matter **21**, 204101 (2009).
[28]J. T. Padding and W. J. Briels, J. Chem. Phys. **132**, 054511 (2010).
[29]R. L. C. A. Akkermans and W. J. Briels, J. Chem. Phys. **113**, 6409 (2000).
[30]J. T. Hynes, Annu. Rev. Phys. Chem. **28**, 301 (1977).
[31]S. H. Lee and R. Kapral, J. Chem. Phys. **121**, 11163 (2004).
[32]T. Bohlin, Trans. Roy. Inst. Technol. (Stockolm) no. 155 (1960).
[33]G. M. Mavrovouniotis and H. Brenner, J. Colloid Interface Sci. **124**, 269 (1988).
[34]J. Happel and E. Bart, Appl. Sci. Res. **29**, 241 (1974).
[35]S. Bhattacharya, J. Blawzdziewicz, and E. Wajnryb, Physica A **356**, 294 (2005).